Nanoscale

PAPER

View Article Online
View Journal | View Issue

Cite this: *Nanoscale*, 2026, **18**, 5517

Long-term exposure to nanoparticles alters senescence-associated markers and immune responses in human monocyte-derived macrophages

Henry Lee, [a] Moritz Häffner,[a] Sandor Balog, [a,b] Patricia Taladriz-Blanco, [a] Aurélien Mroczek,[a] Simona Staudinger,[a,c] Alke Petri-Fink [a] and Barbara Rothen-Rutishauser *[a]

Background: Macrophages are essential in maintaining tissue homeostasis. However, their functionality and phenotype can be impaired by senescence, which impacts immune competence and inflammatory responses. Despite the growing use of engineered nanoparticles (NPs) in biomedical applications or chronic exposure to environmental NPs, their impact on macrophage senescence and immune function remains poorly understood, particularly in the context of prolonged NP exposure. *Results*: Here, we first confirm that human monocyte-derived macrophages (MDMs) undergo senescence *in vitro*, as indicated by a panel of senescence-associated markers that increased within 10 days of culture. Then, we investigate how gold (AuNPs), silica (SiO_2 NPs), and polyethylene terephthalate (PET NPs) influence senescence-associated markers, and immunocompetence in MDMs. By examining key markers such as senescence-associated beta-galactosidase (SA-β-gal), *CDKN2A* (p16), and senescence-associated secretory phenotype (SASP) cytokines, *e.g.*, interleukin (IL)-6 and IL-8, over extended exposure periods up to 10 days, we revealed material-specific effects: AuNPs induce a strong pro-inflammatory response, SiO_2 NPs demonstrate low inflammatory potential, and PET NPs modulate the gene expression level of *CDKN2A* involved in cell cycle regulation. *Conclusion*: Our findings underscore the need to characterize long-term NP behavior in biological systems and reveal material-specific effects on macrophage senescence-associated traits and immune function. Rather than assessing NP-induced senescence, this study defines how prolonged NP exposure modulates selected senescence-associated signatures in non-proliferative macrophages, offering valuable insights into the functional consequences of chronic NP accumulation.

Received 29th November 2025,
Accepted 3rd February 2026

DOI: 10.1039/d5nr05035a

rsc.li/nanoscale

Introduction

Cellular senescence is a state of irreversible growth arrest[1] that arises as a result of various forms of cellular stress, including DNA damage, oxidative stress, and oncogene activation.[2–4] These stressors trigger complex signaling pathways that lead to the acquisition of distinct hallmarks by senescence cells, such as flattened and enlarged cell morphologies with modified cytoplasmic compositions. A key senescence marker is the presence of elevated β-galactosidase (β-gal) activity, which is widely used to identify senescent cells.[5,6] One of the most critical molecular events in the establishment of senescence is the upregulation of the cyclin-dependent kinase (CDK) inhibitor levels, including p21 (CDKN1A) and p16 (*CDKN2A*).[7] Elevated levels of p21 and p21 prevent the phosphorylation of the retinoblastoma protein (Rb), thereby locking the cell in a permanent cell cycle arrest.[8] Although this growth arrest serves as a protective mechanism to prevent the proliferation of damaged cells, the accumulation of senescent cells over time contributes to the onset of age-related diseases.[9,10] Senescent cells secrete a host of pro-inflammatory cytokines, chemokines, and matrix-degrading enzymes, collectively known as the senescence-associated secretory phenotype (SASP), which can disrupt tissue homeostasis and drive chronic inflammation.[11] The ability of senescent cells to promote systemic aging and pathology, including cardiovascular disease,[12] pulmonary fibrosis,[13] osteoarthritis,[14] and neurodegeneration,[15,16] has made them an attractive target for therapeutic interventions.[17,18]

In recent years, nanotechnology has emerged as a promising tool, particularly for the selective targeting and removal of

[a]*Adolphe Merkle Institute, University of Fribourg, SwitzerlandChemin des Verdiers 4, Fribourg, Switzerland. E-mail: barbara.rothen@unifr.ch*
[b]*National Center of Competence in Research Bio-Inspired Materials, University of Fribourg, Chemin des Verdiers 4, 1700 Fribourg, Switzerland*
[c]*Department of Health Sciences and Technology, ETH Zurich, Switzerland*

senescent cells.[19,20] Senolytic drugs, designed to eliminate these cells, have shown promise in addressing age-related diseases,[21,22] and interest is growing in using nanoparticles (NPs) to enhance these therapies further.[23] Agostini *et al.* developed mesoporous silica (SiO_2) NPs coated with galacto-oligosaccharides (GOS), releasing therapeutic cargo upon contact with β-gal in senescent cells.[24] Building on this, the encapsulation of the senolytic navitoclax in GOS-coated silica NPs significantly reduced tumor growth and metastasis in murine cancer models.[25] Despite these advances, the effects of NPs on senescent cells remain largely uncharted, though their distinct physicochemical properties hold potential for a range of biomedical applications.[26]

Macrophages, key players in immune surveillance and tissue homeostasis, are among the primary cell types that interact with NPs.[27] The route of administration, whether intravenous, oral, or *via* inhalation, determines the site where macrophages first encounter NPs, influencing how they process, retain, degrade, or excrete them.[28] Notably, macrophages have been shown to undergo senescence in a context-dependent manner, contributing to chronic inflammation and disease progression,[29,30] such as in atherosclerosis[31] and fibrosis.[32] As macrophages play a dual role in immune response and senescence, understanding how they interact with NPs is crucial. Despite the growing interest in senolytic approaches, there is a clear gap in knowledge regarding how NPs alone might influence senescence-associated features in macrophages.

Human monocyte-derived macrophages (MDMs) are widely used to evaluate NPs–macrophage interactions,[33] as they represent the first cell of contact upon NP administration into the bloodstream. In this study, we first confirm that MDMs undergo senescence upon prolonged time in cell culture by analyzing a panel of senescence-associated markers. Second, we investigate the impact of two types of engineered NPs, gold (Au) NPs and amorphous SiO_2 NPs, which are commonly applied in biomedical settings, on senescence-associated markers in MDMs. AuNPs have shown significant potential in therapeutic applications, including drug delivery and photothermal therapy, due to their biocompatibility and ease of functionalization.[34] SiO_2 NPs, commonly found in pharmaceutical products, are widely used in various industries, making their effects on human health an important study area.[35] In addition, we also explore the effects of polyethylene terephthalate (PET) NPs, a type of nanoplastic derived from either primary production or the degradation of recycled plastic waste.[36] PET NPs have garnered attention due to their increasing detection in the human bloodstream,[37,38] raising urgent concerns about their potential impact on human health. Unlike inorganic NPs, PET NPs represent a different category of environmental contaminants, and their long-term effects, particularly on cellular aging processes and senescence, remain poorly understood. By assessing the expression of key senescence markers, including senescence-associated beta-galactosidase (SA-β-gal) activity and *CDKN2A* (p16), as well as the secretion of SASP factors such as interleukin (IL)-6 and IL-8, we explore how different NPs exposure conditions of up to 10 days, both acute and continuous, influence macrophage senescence. These specific senescence-associated markers were chosen because *CDKN2A* (p16) reflects the cell-autonomous cell-cycle regulatory arm of senescence,[39] while *IL-6* and *IL-8* are key SASP cytokines that capture the non-cell-autonomous inflammatory component of senescence.[40] Together, this focused panel provides a coherent readout tailored to our aim of assessing how long-term NP exposure modulates senescence-associated markers in macrophages rather than defining a complete SASP profile. For inorganic NPs like AuNPs and SiO_2 NPs, the focus lies on their implications in nanomedicine, particularly how their internalization might induce or modulate senescence-associated pathways. Meanwhile, for PET NPs, the study investigates their potential role as environmental stressors, shedding light on their impact on cellular aging. Once internalized, this research provides critical insights into how these diverse classes of NPs affect cellular senescence, filling a significant gap in nanomedicine and environmental health sciences.

Materials and methods

Synthesis of gold nanoparticles

15 nm AuNPs, which served as seeds, were synthesized by boiling a 0.5 mM solution of gold salt (tetra chloroauric acid, HAuCl4·3H_2O, 99%, Sigma-Aldrich, Switzerland) in a 1.5 mM sodium citrate solution (C6H5Na3O7·H_2O, 98%, Sigma-Aldrich, Switzerland).[41] The resulting dispersion was cooled to room temperature and stored in the refrigerator until further use. Following Brown *et al.*,[42] a seeded growth method was employed to prepare AuNPs with a diameter of approximately 41 nm. In this procedure, a reaction mixture consisting of 0.25 mM gold salt, 15 nm gold seed particles (0.0125 mM), and 0.5 mM sodium citrate was stirred, while 1.34 mL of 0.22 M hydroxylamine hydrochloride (NH_2OH·HCl, ACS reagent ≥99%, Sigma-Aldrich, Switzerland) was gradually added. The resulting AuNPs were purified by centrifugation at 3500 rpm for 20 minutes, washed, and resuspended in a 1 mM sodium citrate solution. The concentration of AuNPs was determined by analyzing their UV-Vis extinction spectra, measured at 25 °C using Suprasil-grade quartz cuvettes with a 10 mm optical path length. The spectra were recorded with a Jasco V-670 spectrophotometer (Hellma Analytics, Plainview, NY, USA).

Synthesis of fluorescently labeled silica nanoparticles

Fluorescently labeled SiO_2 NPs (SiO_2-BDP FL, approximately 66 nm in diameter[43,44]) were prepared following a modified Stöber method.[45] Initially, a reaction mixture comprising 6.75 mL of Milli-Q water, 104 mL of absolute ethanol (VWR, Dietikon, Switzerland), and 3.9 mL of 25% ammonium hydroxide (NH4OH) (Merck, Zug, Switzerland) was heated to 60 °C in a 500 mL round-bottom flask equipped with a reflux system for 30 minutes. Subsequently, 11 mL of tetraethyl orthosilicate (TEOS) was added to the solution *via* a syringe. Two minutes

later, a mixture of 200 μL BODIPY FL *N*-Hydroxysuccinimide (NHS) ester (10 mg mL^{-1} in dimethyl sulfoxide (DMSO), Lumiprobe, Hunt Valley, MD, USA) and 4 μL (3-aminopropyl) triethoxysilane (APTES) was introduced into the reaction.

The reaction was allowed to proceed at 60 °C for 4 hours, after which the solution was cooled to room temperature. The NPs were purified by dialysis against Milli-Q water for five days using a 0.2 μM cellulose acetate filter and stored in the dark at 4 °C. The particle concentration was determined by measuring the dry weight of suspensions after evaporating the water at 70 °C.

Synthesis of fluorescently labeled PET nanoparticles

PET nanoparticles were prepared as described by Muff *et al.*[46] Briefly, 5 mg mL^{-1} PET pellets (Goodfellow Cambridge Ltd, Huntingdon, UK) were dissolved in HFIP (TCI, Tokyo, Japan) using a mechanical shaker for two days. A solution of Rhodamine B (Sigma-Aldrich, Burlington, Massachusetts, USA) in ethanol (Sigma-Aldrich, Burlington, Massachusetts, USA) was added to a final concentration of 50 μg mL^{-1}. The polymer–dye mixture and Milli-Q water were manually injected into the CIJ mixing chamber and collected in a 50 mL round-bottom flask containing 12 mL of Milli-Q water under magnetic stirring at 1000 rpm. The dispersion was transferred into a 12–14 kDa dialysis membrane (Carl Roth, Karlsruhe, Germany) and dialyzed against 2 L of Milli-Q water for 48 h, with the water exchanged every 12 h. The nanoparticles were stored in a glass vial and left to sediment for over 24 hours, after which the supernatant containing the PET nanoparticles used in this study was collected and transferred into a new glass vial. The preparation was performed under dark conditions to prevent fluorophore bleaching.

Characterization of PET nanoparticles

Nanoparticle Tracking Analysis (NTA) was used to evaluate particle size distribution and concentration in the dispersion using a Panalytical NanoSight NS500Z (Malvern Instruments, UK) equipped with a 488 nm excitation laser. The camera level was set to 3, screen gain to 2, and detection threshold to 15. Before analysis, the dispersion was diluted 25-fold in Milli-Q water and injected into the glass flow cell at an infusion speed of 1000. Samples were measured in triplicate, and five videos of 5 minutes each were recorded per replicate. These parameters were selected to minimize the influence of particles in the Milli-Q water. The concentration in mass per volume was calculated based on the NTA results (Table S2). An Alpha300 Access confocal Raman microscope (WITec, Ulm, Germany) was used to confirm the chemical composition of the PET nanoparticles. A 785 nm laser and a 50× objective were used, with a laser power of 10 mW, 100 scans, and an integration time of 0.5 s, on a 20 μL PET droplet drop-cast on a silicon wafer (Fig. S3).[47] The hydrodynamic diameter of PET nanoplastics was assessed using dynamic light scattering (DLS) with an Anton Paar Litesizer 500 particle analyzer (Anton Paar, Graz, Austria). Measurements were performed in disposable plastic cuvettes (Carl Roth, Karlsruhe, Germany) using a 1 : 100 diluted sample in Milli-Q water (final volume: 1.2 mL) at 25 °C, with an equilibration time of 30 seconds. The scattering angle was set to 175°, and a 40 mW semiconductor laser centered at 658 nm was used to collect 15 repetitions, each lasting 30 seconds. Transmission and scanning electron microscopy (TEM and SEM) were used to visualize the PET NPs. TEM visualization was performed using a Tecnai Spirit transmission electron microscope (FEI, Hillsboro, OR, USA) operating at 120 kV. Samples were prepared by drop-casting 5 μL of the dispersion onto a carbon film on a copper 300 square mesh grid (Electron Microscopy Sciences, Pennsylvania, PA, USA) and drying at room temperature. Particles were imaged using a 2048 × 2048 pixel wide-angle Veleta CCD camera (Olympus, Tokyo, Japan). Size analysis was conducted manually in Fiji (ImageJ, Wayne Rasband, National Institute of Health, USA) by measuring the maximum diameter of each particle. A 3D view of the particles was obtained using a TESCAN Mira 3 LM field emission SEM (Kohoutovice, Czech Republic). Briefly, 10 μL of the dispersion was dried at room temperature on a silicon wafer affixed to aluminum SEM stubs (Agar Scientific, UK) with double-coated copper conductive tape (Ted Pella, Redding, California, USA). The dried particles were sputter-coated with a 2.5 nm layer of gold using a 208 HR sputter coater (Cressington Scientific Instruments, Watford, UK).

Physicochemical characterization

The NPs were visualized using a Tecnai Spirit TEM operating at an acceleration voltage of 120 kV (FEI, Columbia, MD, USA). The core diameter and size distribution of AuNPs and SiO_2 NPs were calculated using an open-source image processing program (ImageJ, Wayne Rasband National Institute of Health, Bethesda, MD, USA[48]). The hydrodynamic diameter of the nanoparticles was determined with the Anton Paar Litesizer 500 particle analyzer (Anton Paar, Graz, Austria). Measurements were conducted in Milli-Q water at 25 °C and in complete cell culture media after incubation at 37 °C for 0 hours, 24 hours, 5 days, and 10 days.

Dosimetry of engineered nanoparticles in complete cell culture media

To determine the cellular dose of NPs *in vitro*, the *In vitro* Sedimentation, Diffusion, and Dosimetry (ISDD) model was employed.[49] This computational approach calculates particle transport in cell culture media to cells in monolayer cultures.

Endotoxin content

Per the manufacturer's guidelines, the endotoxin levels in the NP suspensions were measured using the Pierce™ LAL Chromogenic Endotoxin Quantitation Kit (ThermoFisher Scientific, Basel, Switzerland). The endotoxin concentration in these suspensions was below 0.5 EU mL^{-1}.

Cell culture

The study involving primary human MDMs was approved by the Federal Office for Public Health Switzerland (reference number: 611-1, Meldung A110635/2). Macrophages were gener-

ated from buffy coats supplied by Interregionale Blutspende SRK AG, Bern, Switzerland, following an established protocol. Peripheral blood mononuclear cells (PBMCs) were separated from human blood using a density gradient medium (Lymphoprep, Grogg Chemie, Stettlen, Switzerland). Monocytes were subsequently isolated and purified using CD14+ magnetic beads (Miltenyi Biotec GmbH, Bergisch Gladbach, Germany), adhering to the manufacturer's instructions. These monocytes were cultured in Roswell Park Memorial Institute (RPMI-1640) medium supplemented with 10% fetal bovine serum (FBS), 2 mM L-glutamine, and penicillin/streptomycin (100 U mL^{-1} and 100 μg mL^{-1}, respectively). Cultures were maintained at a density of 10^6 cells per mL in the presence of 10 ng mL^{-1} macrophage colony-stimulating factor (M-CSF; Miltenyi Biotec) for six days. After differentiation, cells were seeded in 6-well plates (Corning, USA). After 6–7 days of M-CSF differentiation, human MDMs are fully mature and non-proliferative, in agreement with their terminally differentiated state.

Assessment of cell morphology, cell death, and particle detection in cells by confocal microscopy

Macrophages (120 000 cells per well) were seeded in 8-well μ-slides (ibidi) and exposed to AuNPs, SiO_2 NPs, or PET NPs at 20 μg mL^{-1} under specified conditions alongside appropriate controls. β-galactosidase staining (BioTracker™ 510 Green β-Gal Dye, Merck Millipore) and cell viability staining (ReadyProbes® Cell Viability Imaging Kit, Thermo Fisher Scientific) were conducted according to the manufacturer's instructions, with live imaging performed immediately post-staining. SA-β-Gal activity was assessed only in NP-free macrophages to avoid misinterpretation due to fluorescence interference and NP-driven lysosomal alterations, both of which are known to compromise the specificity of this assay in macrophage–NP systems. For other assays, cells were washed with PBS, fixed with 4% paraformaldehyde (PFA) for 15 minutes at room temperature, and washed thrice with PBS. Finally, 300 μL of PBS was added to each well for imaging with a Leica Stellaris 5 confocal microscope.

Focused ion beam-scanning electron microscopy sample preparation

Macrophages were cultured in 35 mm glass-bottom dishes (MatTek Inc., Ashland, MA, USA) and exposed to 20 μg mL^{-1} of AuNPs, SiO_2 NPs, or PET NPs for 10 days. Fixation was performed with 2% paraformaldehyde and 2.5% glutaraldehyde in PBS on ice for 2 hours. After washing with 0.2 M cacodylate buffer (Electron Microscopy Sciences), the samples were incubated with 3% potassium hexacyanoferrate(II) trihydrate and 0.25% osmium tetroxide in cacodylate buffer for 1 hour on ice. The samples were treated with thiocarbohydrazide followed by osmium tetroxide and then dehydrated using graded ethanol and 100% acetone. In increasing concentrations, samples were infiltrated with Epon resin and polymerized at 60 °C for 48 hours. After detachment and sputter-coating with gold, samples were imaged.

FIB-SEM cross-sections

Cross-sectional imaging using FIB-SEM was carried out with a Thermo Scientific Scios 2 Dual Beam microscope (Thermo Fisher Scientific, Waltham, MA, USA). A platinum (Pt) layer of 1 μm thickness was deposited using a 30 kV acceleration voltage and a 1 nA current to protect the selected cell. A trench with a depth of 5 μm was then milled around the cell's front face and sides utilizing the ion beam operating at a 7 nA current. Subsequently, the newly exposed surface of the cell was polished using the ion beam at a current of 1 nA and a voltage of 30 kV. Imaging parameters were set with an electron beam acceleration voltage of 5 kV, a current of 0.4 nA, a resolution of 1536 × 1024 pixels, and a dwell time of 45 μs. All images were captured in immersion mode using a backscattered electron detector.

Inductively coupled plasma-optical emission spectra to determine AuNPs per cell

To determine the number of AuNPs per cell, exposed cells were washed three times with PBS, detached mechanically using 1 mL of PBS, and transferred to 15 mL Falcon tubes. Ten microliters of the suspension were used for cell counting. After centrifugation at 300*g* for 5 minutes, the supernatant was discarded, and cell pellets were stored at −80 °C. For digestion, the samples were thawed incrementally, then resuspended in 300 μL of a mixture of H_2O_2 : HNO_3 (2 : 1, Sigma-Aldrich, USA) and incubated overnight at room temperature. The following day, 400 μL of HCl (37%, VWR, USA) was added and incubated overnight. Samples were diluted to a total volume of 10 mL with Milli-Q H_2O. Analysis was performed using ICP-OES (Optima 7000 DV, PerkinElmer, USA) with a gold standard calibration curve (0–7 mg L^{-1}, Sigma-Aldrich, USA). Operating conditions included a radio frequency power of 1500 W, a plasma gas flow of 8 L min^{-1}, an auxiliary gas flow of 0.2 L min^{-1}, and a pump flow of 0.7 L min^{-1}. Measurements were taken at 1 L min^{-1} with a 15 second equilibration delay. The total gold mass was determined by adjusting for blank corrections and dilution factors. To estimate the number of AuNPs per cell, the total gold mass was divided by the mass of an individual AuNP. This number was further divided by the counted cells per sample to obtain the average number of AuNPs per cell.

Median fluorescence intensity per cell by flow cytometry

Cells were washed with PBS and incubated with 1 mL of Accutase™ (Thermo Fisher Scientific, cat. no. 00-4555-56) for 15 minutes at 37 °C. The cells were detached using a cell scraper in 1 mL of flow cytometry buffer and collected into 5 mL polystyrene round-bottom flow cytometry tubes (Corning® Falcon, Switzerland). The supernatant was discarded after centrifugation at 300*g* for 5 minutes. Cells were stained with DAPI (0.5 μg mL^{-1}) on ice for 10 minutes to assess viability. After washing with 3 mL of flow cytometry buffer, cells were centrifuged again, resuspended in 200 μL of buffer, and analyzed using a full-spectrum flow cytometer (Aurora, Cytek® Biosciences, USA).

RNA isolation, cDNA synthesis, and real-time qRT-PCR analysis

Following NPs exposure, cells were lysed directly in wells using 250 μL of BL + TG buffer (Promega, Madison, WI, USA), and total RNA was extracted using the ReliaPrep™ RNA Cell Miniprep System (Promega, Z6012, Madison, WI, USA). RNA concentration and quality were verified using a NanoDrop™ 2000 spectrophotometer (Thermo Scientific) and an Agilent 2100 Bioanalyzer (Agilent Technologies, Santa Clara, CA, USA), with samples required to have an OD 260/280 ratio ≥1.8. Reverse transcription was performed using the Omniscript RT system (Qiagen, Germany), oligo-dT primers (Microsynth, Switzerland), and RNasin Plus RNase Inhibitor (Promega, USA). The reaction mixture contained 250 ng of RNA, oligo-dT primer, RNase inhibitor, dNTP mix, Omniscript reverse transcriptase, and buffer RT in appropriate proportions. Real-time PCR was conducted with the 7500 Fast Real-Time PCR System (Applied Biosystems, USA) using Fast SYBR Green master mix. Relative gene expression levels were calculated using the ΔΔCt method, normalized to housekeeping genes, and expressed as fold changes ($2^{-\Delta\Delta Ct}$).

Enzyme-linked immunosorbent assay

After NPs exposure, macrophages were stimulated with 2 ng mL^{-1} lipopolysaccharide (LPS) in cRPMI for 24 hours. Supernatants were collected and stored at −80 °C until analysis. According to the manufacturer's protocol, cytokine levels (*IL-6* and *IL-8*) were measured using Human DuoSet ELISA kits (R&D Systems, Switzerland). Samples were analyzed in triplicates and diluted as required (1 : 4 for *IL-6* and 1 : 10 for *IL-8*). Cytokine concentrations were calculated based on a standard curve, and freshly differentiated macrophages treated with LPS served as a positive control.

Statistical analyses

All biological experiments except for imaging were performed with at least three biologically independent replicates from different donors. Statistical significance between conditions was determined using a one-way ANOVA followed by Dunnett's and Tukey's *post hoc* tests for multiple comparisons with a significance level of $p < 0.05$. Analyses were performed using Prism 8 (GraphPad Software).

Results

Assessment of senescence-associated markers in primary human MDMs

The presence and extent of cellular senescence in primary human MDM were evaluated through morphological analysis and senescence-associated beta-galactosidase (SA-β-gal) by LSM at the cultivation time points of day 0 (control), day 5, and day 10 (Fig. 1A). Brightfield images (upper row) show distinct morphological changes by day 10, with macrophages becoming rounder, larger, and flatter than the control, with more elongated cells. While no SA-β-gal was detected in the control (lower row), its presence was detectable from day 5. Furthermore, a magnified image of SA-β-gal-stained macrophages after 10 days of cultivation (Fig. 1B) reveals a vesicular pattern indicating the specificity of the staining and its localization in endolysosomal compartments. Additionally, the gene expression levels of *CDKN2A*, encoding for

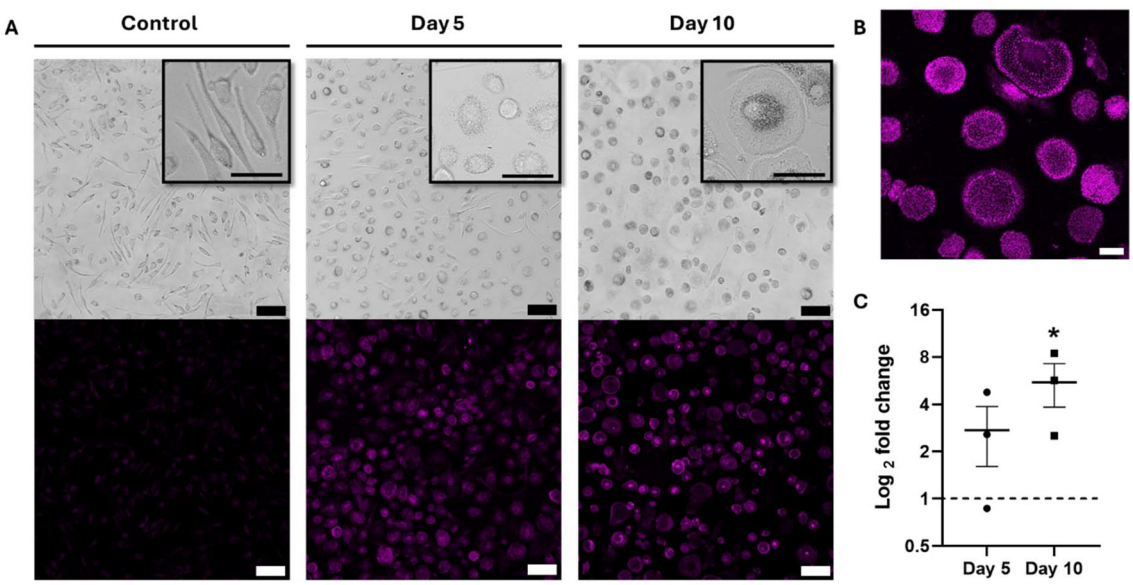

Fig. 1 Characterization of senescence in macrophages without NPs. (A) Qualitative brightfield observation (upper row) of primary human macrophage morphology and detection of the senescence-associated beta-galactosidase (SA-β-gal; lower row) by laser scanning microscopy (LSM) at cultivation time points of day 0 (control), day 5, and day 10. Scale bars: 100 μm and 50 μm in inset. (B) Magnified image of SA-β-gal-stained macrophages after 10 days of cultivation. Scale bar: 20 μm (C) RT-qPCR results showing gene expression levels of *CDKN2A*, which encodes the cell cycle regulation protein p16, for the control (dashed line) and at 5 and 10 days. Statistical significance was determined by a paired *t*-test ($n = 3$); * $p \leq 0.05$.

the cell cycle regulation protein p16, were determined by qRT-PCR for the control and after 5 and 10 days of cultivation (Fig. 1C). An upward trend in expression was observed, with approximately a 3-fold increase after 5 days and a significant 6-fold increase after 10 days compared to the control (dotted line). Overall, the combination of morphological changes, increased SA-β-gal presence in the endolysosomal compartments, and elevated *CDKN2A* gene expression confirmed that primary human MDMs acquire more pronounced senescence-associated markers over time in culture.

Physicochemical characterization and dosimetry of engineered NPs

For this study, Au, SiO_2, and PET NPs (Fig. 2) were synthesized, and NPs characterization in cell culture media was conducted at a concentration of 20 μg mL^{-1}. Transmission electron microscopy (TEM) images of AuNPs (Fig. 2A & S1A), conducted in water prior to cell culture experiments, revealed well-dispersed spherical particles with a uniform size distribution, resulting in a core diameter of 41 ± 4 nm (Fig. 2D). Dynamic light scattering (DLS) measurements further confirmed the stability of AuNPs in supplemented cell culture media over 10 days, with a hydrodynamic diameter of 115 ± 7 nm (Fig. S2A and Table S1). Similarly, TEM micrographs of SiO_2 NPs labeled with BODIPY-FL dye (Fig. 2B & S1B), showed spherical particles and a uniform size distribution, yielding a core diameter of 66 ± 8 nm (Fig. 2E). Subsequent DLS measurements revealed changes in particle size during incubation in cell culture media, indicating partial dissolution of SiO_2 NPs over time. By day 10, the particle size was reduced to approximately 35 nm

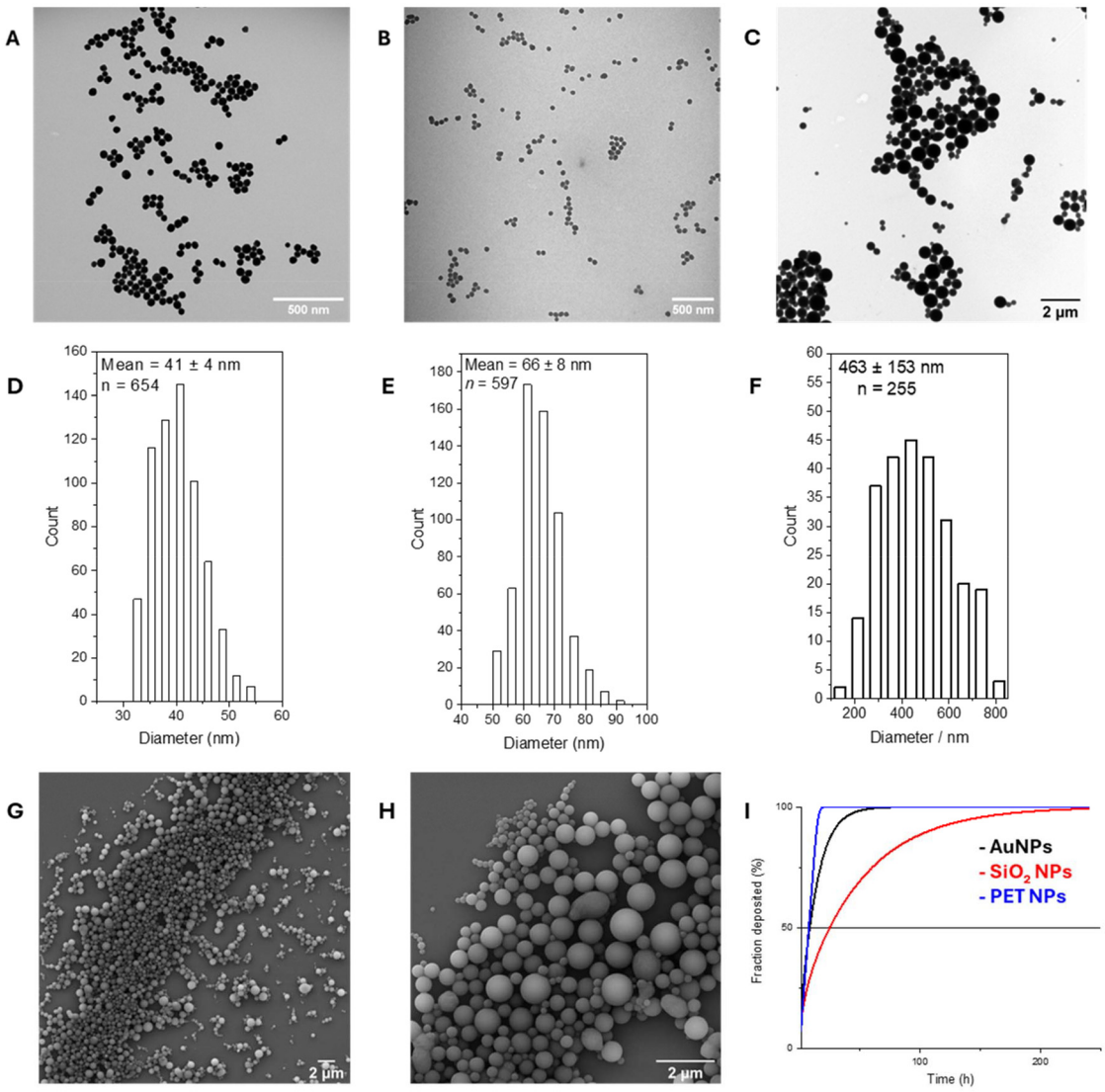

Fig. 2 Characterization of the NPs used in this study and dosimetry. Representative TEM micrographs of AuNPs (A), SiO_2 NPs (B), and PET NPs (C). Size-distribution histograms derived from TEM analysis are shown for AuNPs (D), SiO_2 NPs (E), and PET NPs (F). SEM images of PET NPs at lower (G) and higher (H) magnification illustrate their polydisperse morphology. The dosimetry estimation curves (I) display the predicted fraction of AuNPs (black), SiO_2 NPs (red), and PET NPs (blue) deposited onto the bottom of the culture wells over time. The vertical line indicates the time points at which 50% of each NP population is estimated to have sedimented.

(Fig. S2B and Table S1). 463 nm – PET NPs (Fig. 2C and F–H) labeled with Rhodamine B were synthesized by nanoprecipitation.[46] Their colloidal stability in supplemented cell culture media was assessed using DLS (Fig. S2C and Table S1), which showed no significant increase in size, indicating minimal protein-PET NPs interactions. Nanoparticle tracking analysis (NTA) (Table S2) was employed to determine the concentration of PET NPs in the dispersion. The size results obtained from DLS and NTA in water were comparable, with NTA reporting a mean size of 432 ± 13 nm and D90 of 626 ± 26 nm. Additionally, PET NPs were visualized using scanning electron microscopy (SEM) and TEM. The micrographs corroborated the results from DLS and NTA regarding the polydispersity of the dispersion, revealing spherical particles with a core diameter of 463 ± 153 nm. The hydrodynamic diameter measurements from both DLS and NTA, when compared with TEM observations, indicate the absence of a protein corona on the PET NPs. To further understand NPs behavior in the macrophage culture system, dosimetry estimations were performed to investigate the deposition kinetics of the NPs onto the bottom of the cell culture well where macrophages are present (Fig. 2I). Deposition curves show distinct profiles for each NPs type. AuNPs (black curve) displayed a rapid deposition, with 50% of particles deposited within 8.5 hours and over 98% deposition achieved by 47 hours. SiO_2 NPs exhibited slower deposition (red curve), with 50% deposition occurring after approximately 24 hours and over 98% deposition achieved by 190 hours (8 days). In contrast, PET NPs had the fastest deposition rate, with 50% deposited within 7.5 hours and over 98% deposition achieved by 16.5 hours (blue curve). These distinct deposition profiles suggest that NPs composition and exposure duration may play critical roles in influencing cellular responses.

Investigation of the interaction and uptake of engineered NPs in human MDMs

The interaction and uptake of engineered NPs (AuNPs, SiO_2 NPs, and PET NPs) by human MDMs were evaluated under three distinct exposure conditions: (1) a 5 day continuous exposure with a single application of NPs without media

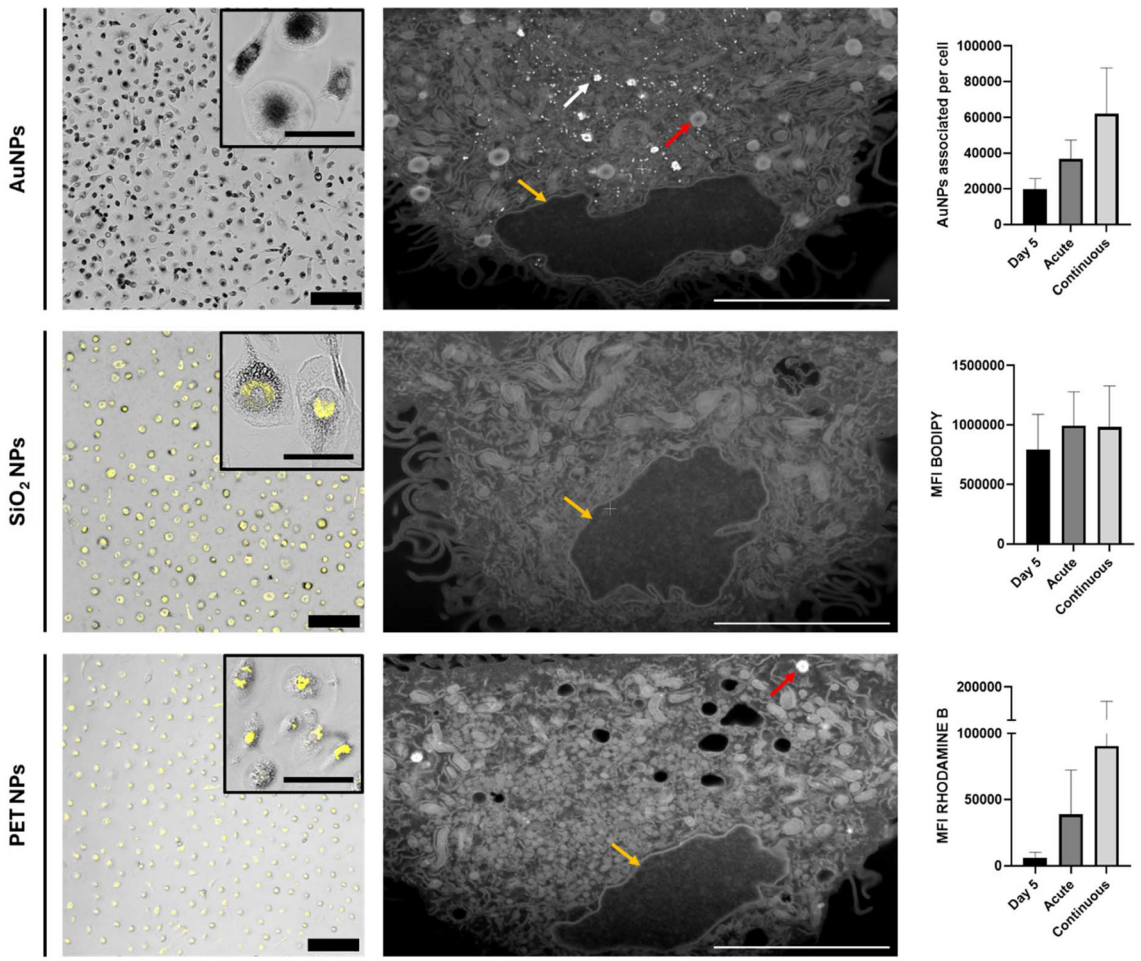

Fig. 3 Assessment of the interaction between AuNPs, SiO_2 NPs, and PET NPs with human MDMs after 10 days. The first column presents the visualization of NPs interacting with macrophages using LSM. Scale bars 100 μm and 50 μm in the inset. The middle column displays cross-sections of the macrophages captured by FIB-SEM. White arrows denote NPs, red arrows indicate lipid droplets, and yellow arrows highlight the nucleus. Scale bar: 5 μm. Quantitative uptake was measured using ICP-OES for AuNPs and flow cytometry for SiO_2 and PET NPs after 5 and 10 days of exposure, under both acute (24 h NPs exposure followed by medium replacement) and continuous (no medium change) conditions.

change, (2) a 10 day continuous exposure under the same conditions, and (3) an acute 24 hour exposure followed by washing and replacement with NP-free media for the subsequent 9 days. These experimental setups were designed to compare the short-term and prolonged effects of the NPs on macrophage behavior. A combination of imaging and analytical techniques was used to investigate NPs-cell interactions, with the results presented in a multi-panel figure (Fig. 3). The figure is organized by columns (displaying laser scanning microscopy (LSM) images, focused ion beam scanning electron microscopy (FIB-SEM) cross-sections, and quantification data) and rows corresponding to each NPs type. Quantification was performed using inductively coupled plasma optical emission spectroscopy (ICP-OES) for AuNPs, while fluorescently labeled SiO_2 and PET NPs were (semi)-quantified using flow cytometry.

For AuNPs, LSM revealed clear evidence of internalization or cell association after 10 days, which is defined as NPs being bound to the cell surface or internalized. The strong optical contrast of AuNPs facilitated their visualization. Live/dead staining, analyzed *via* LSM, confirmed minimal cell death, with no significant differences in viability compared to controls (Fig. S2B). FIB-SEM cross-sectional imaging further supported these findings, showing healthy macrophages with intracellular AuNPs, indicating effective internalization without compromising cell viability. Although donor-to-donor variability prevented statistical significance, ICP-OES analysis revealed that 10 days of continuous exposure led to the highest level of cell-associated AuNPs, with an average of approximately 60 000 particles per cell. Interestingly, acute exposure for 10 days resulted in a higher number of cell-associated NPs than 5 days of continuous exposure, suggesting a distinct temporal pattern of uptake.

LSM imaging showed the accumulation of SiO_2 NPs within macrophages after 10 days. Due to their small size and low electron scattering capacity, SiO_2 NPs were not directly visible *via* FIB-SEM imaging. However, macrophages displayed no structural abnormalities at the EM resolution. Live/dead staining confirmed that SiO_2 NPs did not induce significant cell death after 10 days of exposure (Fig. S2C). Flow cytometry results indicated that both acute and continuous 10 day exposures resulted in higher intracellular SiO_2 NP signals compared to the 5 day condition. Unlike AuNPs, no clear difference emerged between the two 10-day SiO_2 NP exposure scenarios, which may reflect progressive slow dissolution of the silica shell over time, resulting in reduced detectable fluorescence and diminished differences in apparent uptake.

PET NPs also demonstrated significant interaction with macrophages. LSM imaging revealed a high level of PET NP accumulation within cells after 10 days of exposure. Importantly, macrophages exhibited a normal morphology without any signs of structural alterations while acquiring the characteristic flatter and larger morphology typically associated with senescence, similar to what was observed with the other NPs, as confirmed by LSM and FIB-SEM imaging. FIB-SEM revealed densely packed, spherical structures within cytoplasmic compartments, likely representing PET NPs, though definitive identification was limited due to the carbon-based nature of PET. Live/dead staining confirmed minimal cell death, indicating preserved cell integrity (Fig. S2D). Flow cytometry showed a progressive increase in NP uptake, with the highest levels observed after 10 days of continuous exposure, followed by acute exposure and 5 days of continuous exposure. This uptake trend mirrored the patterns observed for AuNPs and SiO_2 NPs.

Overall, AuNPs, SiO_2 NPs, and PET NPs were readily internalized by macrophages with no evidence of cytotoxicity. While the differences did not reach statistical significance, intracellular NP levels tended to be highest after 10 days of continuous exposure, with lower levels observed in the acute and 5 day conditions. These trends indicate that prolonged exposure may result in r NP accumulation.

Gene expression levels of senescence-associated markers in macrophages exposed to engineered NPs

Gene expression levels of *CDKN2A*, *IL-8*, and *IL-6* in human macrophages were assessed *via* RT-qPCR following exposure to AuNPs, SiO_2 NPs, and PET NPs (20 μg mL^{-1}) under three conditions: acute (24 hour exposure followed by media replacement and post-exposure for 9 days) and continuous (no media change), after 5 and 10 days. Exposure to AuNPs for 5 days showed a trend toward lower *CDKN2A* expression and a 4-fold increase in *IL-8*, while *IL-6* displayed an upward tendency compared to controls. This pattern persisted at the 10 day time point, with continuous exposure amplifying these effects. Notably, *IL-6* expression increased 5-fold under continuous exposure compared to acute conditions, further underscoring the impact of prolonged AuNPs exposure. In contrast, SiO_2 NPs induced a distinct gene expression profile. After 5 days, *CDKN2A* was significantly upregulated, while *IL-8* and *IL-6* were minimally affected. After 10 days, acute exposure led to significant downregulation of *IL-8*, while continuous exposure caused a downregulation of *CDKN2A*. The remaining genes displayed no substantial changes, regardless of the exposure scenario. For PET NPs, a significant downregulation of *CDKN2A* was observed after 5 days, while *IL-8* and *IL-6* remained unchanged. After 10 days, both exposure types led to pronounced *CDKN2A* downregulation, and continuous exposure significantly increased *IL-6* expression. Despite these findings, donor-to-donor variability was observed across experiments. These results highlight that the expression of senescence-associated *CDKN2A* and the SASP-related genes *IL-8* and *IL-6* are differentially modulated by the type of NPs and the exposure conditions, revealing nuanced effects on macrophage gene regulation (Fig. 4).

Immunocompetence of NPs-exposed macrophages

The levels of *IL-8* and *IL-6* in the supernatant were quantified *via* ELISA following macrophage exposure to AuNPs, SiO_2 NPs, and PET NPs at 20 μg mL^{-1} under varying exposure conditions. To assess the inflammatory potential of the NPs and the capacity of macrophages to respond to an external immune stimulus, cells were subsequently stimulated with lipopolysaccharide (LPS, 2 ng mL^{-1}) on day 4 or day 9. Notably, both acute and continuous exposure to AuNPs resulted in an elevated release of IL-8 compared to controls, with the most pro-

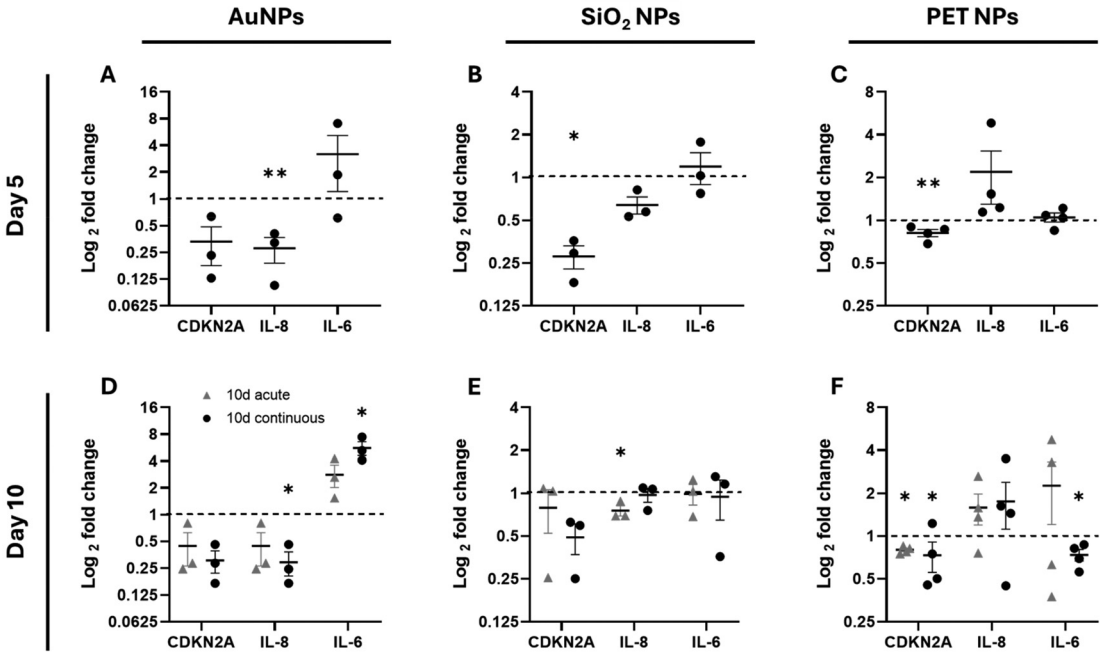

Fig. 4 Gene expression levels of *CDKN2A*, *IL-8*, and *IL-6* in human monocyte-derived macrophages after exposure to Au, SiO_2, and PET NPs (20 μg mL^{-1}). Macrophages were exposed to Au, SiO_2, and PET NPs for 5 days (A–C) and 10 days (D–F) under two conditions: acute exposure (24 h NPs exposure followed by medium replacement) and continuous exposure (no medium change). Gene expression was assessed using RT-qPCR, and values plotted are expressed as $2^{-\Delta\Delta CT}$. Data are presented as individual values with mean ± SEM ($n \leq 3$). Statistical analysis was performed using the ΔCT values, with a paired *t*-test comparing NPs-exposed cells to the control group (dotted line); * $p \leq 0.05$, ** $p \leq 0.01$.

nounced effect observed under continuous exposure over the 5 day period. However, after 10 days, neither exposure condition showed significant changes in *IL-8* levels. Regarding *IL-6*, similar trends were noted across both 5 and 10 day exposures, where continuous exposure elicited the highest release, followed by acute exposure, compared to controls. For SiO_2 NPs, LPS-induced *IL-8* release remained largely unaffected by the NPs. However, acute exposure led to a marked increase in *IL-8* after 5 and 10 days relative to controls and continuous exposure. Interestingly, after 5 days, *IL-6* levels were significantly lower in the acute condition compared to controls, while the opposite pattern emerged after 10 days. Continuous exposure to SiO_2 NPs did not significantly affect *IL-6* release at either time. Exposure to PET NPs had minimal impact on the LPS-induced immune response for both *IL-8* and *IL-6* after 5 days. However, after 10 days, a reduction in *IL-8* release was observed, particularly under acute exposure conditions. *IL-6* releases remained largely unaffected by PET NPs after 10 days. In conclusion, the LPS-triggered release of *IL-8* and *IL-6* varied significantly depending on the NPs type and exposure duration, highlighting distinct immune response patterns associated with each material (Fig. 5).

Discussion

The progressive accumulation of senescent cells with aging significantly contributes to the decline in tissue function and the onset of various age-related diseases,[50] emphasizing the need to understand how different external factors may influence cellular senescence. With the rapid rise in the use of NPs in medicine and occupational exposure,[51] these particles have become an increasingly prevalent, though poorly understood, factor in aging biology. Previous studies have primarily explored NPs-induced senescence in lung and fibroblast cell lines, focusing on carbon and silver NPs as triggers of premature cellular aging.[52,53] These findings were derived from a limited range of cell types and have not yet been extended to immune cells, particularly human-derived macrophages. Our study aimed to elucidate the impact of engineered NPs (AuNPs, SiO_2 NPs, and PET NPs) on senescence-associated markers in human MDMs, focusing on key markers such as SA-β-gal, *CDKN2A* (p16), and the SASP-related cytokines *IL-6* and *IL-8*. The findings revealed important insights into how NPs, widely used in therapeutic and NPs exposure to humans in an occupational context, can influence macrophage senescence markers and immune function.

The variations observed in gene expression and immune responses, especially in response to LPS stimulation, highlight that individual immune profiles and genetic backgrounds can significantly shape how macrophages respond to different NPs. However, one consistent finding was the effect of AuNPs: they led to a time-dependent increase in *IL-6* levels under untreated and LPS-stimulated conditions. This indicates a clear pro-inflammatory effect specific to AuNPs, distinguishing them from SiO_2 and PET NPs. The pattern of *IL-6* elevation

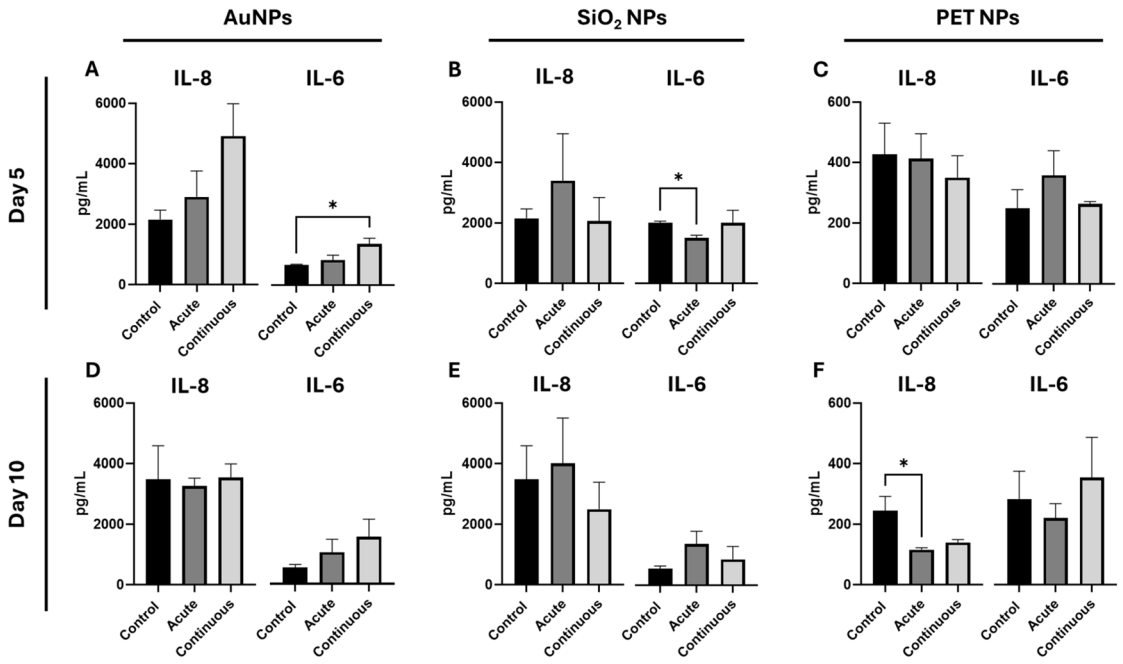

Fig. 5 Immunocompetence of human MDMs after exposure to Au, SiO_2, and PET NPs (20 μg mL^{-1}). Macrophages were treated with AuNPs (A and D), SiO_2 NPs (B and E), or PET NPs (C and F) for 4 days (A–C) and 9 days (D–F) under two exposure conditions: acute exposure, where the medium was replaced after 24 hours of NPs exposure, and continuous exposure, where the cells remained in NPs containing medium without replacement throughout the exposure period. Following these exposures, cells were stimulated with LPS (2 ng mL^{-1}) for 24 hours. IL-8 and *IL-6* levels in the supernatant were quantified by ELISA. Control samples correspond to untreated cells incubated for 4 or 9 days followed by 24 hours of LPS stimulation, depending on the experimental condition. LPS control samples of freshly differentiated MDMs (not shown) exhibited significantly higher cytokine secretion levels for both *IL-6* and IL-8 than NPs-treated and untreated controls. Data are presented as mean ± SEM ($n \leq 3$), and statistical significance was determined using one-way ANOVA followed by Dunnett's multiple comparison tests against the control (untreated cells); * $p \leq 0.05$.

implies that both acute and prolonged exposure to AuNPs may prime macrophages to adopt a pro-inflammatory state even without additional inflammatory triggers.

AuNPs are known to disrupt cellular balance through mechanisms such as DNA damage, oxidative stress, and alterations in gene expression and epigenetic regulation.[54,55] For example, they can activate pathways like NF-κB, which drives the production of pro-inflammatory cytokines such as *IL-6*.[56] Since *IL-6* is a hallmark of the SASP, our findings suggest that chronic exposure to AuNPs may contribute to senescence-like changes by creating a pro-inflammatory environment. This aligns with studies that link NPs-induced stress with increased inflammatory signaling, indicating that AuNPs may promote immune senescence.

In contrast, SiO_2 NPs showed minimal impact on senescence markers, suggesting a lower inflammatory potential. This could position SiO_2 as a more biocompatible option, particularly in applications where reducing inflammatory response is important.

A unique and noteworthy outcome in our study is the effect of PET NPs on *CDKN2A* expression, which encodes the cell cycle inhibitor p16, a known senescence marker. PET exposure consistently lowered *CDKN2A* expression, suggesting that PET may influence regulatory pathways that control cell cycle progression. This decrease in p16 hints that PET could interact with pathways related to cell proliferation or epigenetic mechanisms influencing senescence. Such interactions may be relevant for cellular aging, particularly in immune cells like macrophages, which are critical in immune surveillance and inflammatory response. Further studies could explore these effects by focusing on specific cell cycle and proliferation pathways essential to understanding cellular senescence dynamics.

We also observed mild modulation of immune functions in response to PET NPs, raising questions about the long-term impact of PET exposure on immune health, especially in the context of aging. As macrophages play key roles in initiating and resolving inflammation, any persistent alterations in their function could have lasting effects on tissue health and immune resilience. Additionally, it is important to consider that particle size heterogeneity may have influenced our findings. Differences in NPs size distribution could affect cellular uptake, localization, and biological response,[57] suggesting that material type and particle size are crucial in determining how NPs interact with immune cells. Furthermore, our results show that exposure conditions, whether acute or continuous, had a significant impact on the variation in senescence-associated marker gene expression levels. Because NPs were present for a longer period of time, continuous exposure frequently produced more noticeable changes. The ability of macrophages exposed to NPs to elicit an LPS-triggered immune response

comparable to controls demonstrated that they had maintained their immunocompetence despite these variations.

A crucial aspect of understanding the dynamics of uptake and cell behavior is the interplay between physicochemical properties, exposure scenarios, and cellular interactions. While larger NPs may exhibit faster deposition due to sedimentation, this does not consistently translate to increased cellular uptake or stronger biological responses. This apparent disconnect can be explained by several dynamic processes that influence NPs' behavior over time. One key factor is the balance between endocytosis and exocytosis. As intracellular NPs levels rise, exocytosis increases to balance endocytosis, eventually reaching a transient equilibrium.[58,59] This balance may later shift, with exocytosis dominating and reducing intracellular NPs content.[58,59] A lag between endocytosis and exocytosis could temporarily disrupt equilibrium before stabilizing. In NPs-free conditions, exocytosis initially prevails due to the concentration gradient, followed by a dynamic balance between NPs release and reuptake. Notably, released NPs can be internalized by neighboring cells through transport exocytosis.[60] The tendency of NPs to undergo significant transformations in biological environments, including aggregation and protein corona formation, which affects their bioavailability and cellular interactions, adds another layer of intricacy. Aggregation, influenced by factors like surface properties, exposure duration, and cell membrane tension, can alter NPs uptake.[61,62] Simultaneously, the dynamic formation and evolution of a protein corona on NPs surfaces modify their biological identity, uptake mechanisms, and cellular responses.[63,64] These factors may explain the counterintuitive finding that acute exposure (24 h in NP-containing media followed by 9 days in NP-free conditions) resulted in higher uptake than continuous exposure (5 days without media change). Prolonged exposure allows endocytosis and exocytosis rates to equilibrate, reducing net uptake over time, whereas acute exposure delivers a concentrated NP dose, maximizing initial uptake.

Despite these differences in uptake, there were no consistent changes in senescence-associated markers or immunocompetence of human MDMs between the two exposure scenarios. The critical determinant was NPs exposure condition, highlighting the fundamental role of NPs in modulating cellular responses. However, this study did not explore repetitive NPs exposure, which could result in different biological responses, potentially altering uptake and cellular outcomes. The dissolution of SiO_2 NPs over time adds another layer of complexity to their dosimetry and cellular interactions. As SiO_2 NPs dissolve in biological media,[65] their size and concentration are progressively reduced, leading to a dynamic alteration in their bioavailability. This dissolution process may explain the reduced differences in uptake observed between acute and continuous exposure scenarios for SiO_2 NPs. Over time, the dissolved silica may also contribute to altered cellular responses. PET NPs pose a unique challenge due to their extreme polydispersity, with sizes ranging from 100 nm to 1 μm. Larger particles deposit quickly onto the cell surface, creating higher localized concentrations, while smaller particles remain suspended, prolonging interaction and uptake. This size heterogeneity leads to variable dosimetry and biological effects, emphasizing the need for detailed characterization to interpret results accurately. However, this polydispersity also mirrors real-life exposure to inherently polydisperse plastic particles, making these findings highly relevant for understanding real-world scenarios.

One limitation of our study is the lack of information regarding the age and sex of the donors from whom the human MDMs were derived. Age and sex are critical biological variables that significantly influence immune cell function,[66] including macrophage behavior and responses to external stimuli such as NPs. Macrophages from older individuals or different sexes may exhibit distinct inflammatory profiles, levels of senescence, and immune competence,[67] potentially leading to varying outcomes in response to NPs exposure.[68] These factors could also explain some donor-to-donor variations observed in our results. Future investigations should consider donor age and sex to provide a more comprehensive understanding of how these factors influence macrophage–NPs interactions. This would enhance the applicability of our findings to diverse populations and help uncover potential age- or sex-specific vulnerabilities to NP exposure, aligning with current guidelines that stress the importance of accounting for biological sex and age in experimental design.

Importantly, the use of primary human MDMs represents a relevant system for studying NP behavior. Macrophages are among the first and most abundant cell types to internalize and retain administered NPs *in vivo*, particularly in the liver, spleen, and lung, where long-lived tissue-resident macrophages experience chronic exposure to both engineered and environmental particles. Human MDMs therefore recapitulate key aspects of NP-cell interactions *in vivo*, including phagocytosis, lysosomal processing, cytokine secretion, and long-term intracellular retention. The senescence-associated marker changes and preserved immunocompetence observed in our model provide mechanistic insight into pathways that may similarly be remodeled in macrophages accumulating NP in physiological settings. These signatures offer a focused framework for future investigations in multicellular systems and tissue-resident macrophages.

In this context, an important next step will be to determine the long-term consequences of NP accumulation in macrophages within tissues susceptible to age-related degeneration. Sustained NP exposure may influence the SASP and contribute to chronic inflammatory remodeling, underscoring the need for three-dimensional models and *in vivo* studies. Such approaches will be essential for defining how chronic NP exposure impacts tissue architecture, immune function, and the broader process of organismal aging.

Conclusion

Human MDMs naturally undergo senescence *in vitro*, providing a relevant model to study the effects of NPs on senescence-

associated markers and immunocompetence. Monodisperse and stable AuNPs were found to induce a pro-inflammatory state linked to immune senescence. In contrast, monodisperse SiO_2 NPs, which gradually dissolve over a 10 day incubation period, showed minimal changes in the gene expression of senescence-associated markers. Polydisperse but stable PET NPs influenced cell cycle regulation. Due to the distinct nature of these NPs and the extended timeframes of exposure, it is crucial to thoroughly characterize their long-term behavior in biological environments, *e.g.*, complete cell culture medium, to understand their material-specific effects. Additionally, the observed cellular responses varied depending on the exposure conditions, with notable differences between continuous and acute NP exposure. Finally, macrophages with internalized NPs preserved their immunocompetence, exhibiting no significant deviations in LPS-triggered immune responses compared to the control.

Author contributions

H. L. and B. R-R. designed the project. H. L performed the experiments including the physicochemical characterization (TEM and DLS) of AuNPs, SiO_2 NPs, and PET NPs, cell culture, LSM, FIB-SEM, ICP-OES, flow cytometry, RT-qPCR, ELISA, analyzed the results, and wrote the manuscript; M. H. assisted with the ICP-OES, synthesized the PET NPs, visualized in the TEM and SEM, performed the NTA and QCM measurements, and wrote the materials and methods section about the PET NPs. S. B. performed DLS data and dosimetry analysis; P. T.-B supervised M. H. in preparing and characterizing the PET NPs and analyzed TEM, SEM, NTA, and QCM data of the PET NPs. P. T.-B was responsible for data interpretation regarding all NPs physicochemical properties and manuscript editing. A. P.-F. supervised the project and was involved in the study design and data interpretation; B. R.-R. supervised the project, was involved in the study design, data analysis, and interpretation, and reviewed the manuscript. All authors contributed to the scientific discussions and manuscript revisions. All authors have read and agreed to the published version of the manuscript.

Conflicts of interest

The authors declare no competing interests.

Ethics approval and consent to participate

The study involving primary human MDMs was approved by the Federal Office for Public Health Switzerland (reference number: 611-1, Meldung A110635/2).

Data availability

As part of our commitment to scientific transparency and collaboration, we have decided to upload our data sets to an open repository. By doing so, we aim to make these datasets accessible to the wider scientific community, allowing other researchers to explore and analyze them for further insights.

The data is reposited on zenodo https://doi.org/10.5281/zenodo.14831295.

Supplementary information (SI) is available. See DOI: https://doi.org/10.1039/d5nr05035a.

Acknowledgements

The authors thank Liliane Ackermann Hirschi for nanoparticle synthesis and Shui Ling Chu for help with the cell cultures and ELISA. The authors acknowledge funding from the Swiss National Science Foundation (SNSF) (project 310030_192056/1) and the Adolphe Merkle Foundation. Additionally, this work benefited from support from the Swiss National Science Foundation through the National Center of Competence in Research Bio-Inspired Materials.

References

1 L. Hayflick and P. S. Moorhead, The serial cultivation of human diploid cell strains, *Exp. Cell Res.*, 1961, **25**, 585–621.
2 W. Huang, L. J. Hickson, A. Eirin, J. L. Kirkland and L. O. Lerman, Cellular senescence: the good, the bad and the unknown, *Nat. Rev. Nephrol.*, 2022, **18**, 611–627.
3 H.-L. Ou, *et al.*, Cellular senescence in cancer: from mechanisms to detection, *Mol. Oncol.*, 2021, **15**, 2634–2671.
4 V. Gorgoulis, *et al.*, Cellular Senescence: Defining a Path Forward, *Cell*, 2019, **179**, 813–827.
5 B. Y. Lee, *et al.*, Senescence-associated β-galactosidase is lysosomal β-galactosidase, *Aging Cell*, 2006, **5**, 187–195.
6 G. P. Dimri, *et al.*, A biomarker that identifies senescent human cells in culture and in aging skin in vivo, *Proc. Natl. Acad. Sci. U. S. A.*, 1995, **92**, 9363–9367.
7 G. H. Stein, L. F. Drullinger, A. Soulard and V. Dulić, Differential roles for cyclin-dependent kinase inhibitors p21 and p16 in the mechanisms of senescence and differentiation in human fibroblasts, *Mol. Cell. Biol.*, 1999, **19**, 2109–2117.
8 B. B. McConnell, M. Starborg, S. Brookes and G. Peters, Inhibitors of cyclin-dependent kinases induce features of replicative senescence in early passage human diploid fibroblasts, *Curr. Biol.*, 1998, **8**, 351–354.
9 D. McHugh and J. Gil, Senescence and aging: Causes, consequences, and therapeutic avenues, *J. Cell Biol.*, 2018, **217**, 65.
10 S. He and N. E. Sharpless, Senescence in Health and Disease, *Cell*, 2017, **169**, 1000–1011.

11 J.-P. Coppé, P.-Y. Desprez, A. Krtolica and J. Campisi, The Senescence-Associated Secretory Phenotype: The Dark Side of Tumor Suppression, *Annu. Rev. Phytopathol.*, 2010, **5**, 99.
12 Y. Luan, *et al.*, Cardiac cell senescence: molecular mechanisms, key proteins and therapeutic targets, *Cell Death Discovery*, 2024, **10**, 1–15.
13 M. J. Schafer, *et al.*, Cellular senescence mediates fibrotic pulmonary disease, *Nat. Commun.*, 2017, **8**, 14532.
14 P. R. Coryell, B. O. Diekman and R. F. Loeser, Mechanisms and therapeutic implications of cellular senescence in osteoarthritis, *Nat. Rev. Rheumatol.*, 2021, **17**, 47–57.
15 E. Sikora, *et al.*, Cellular Senescence in Brain Aging, *Front. Aging Neurosci.*, 2021, **13**, 646924.
16 G. Carreno, R. Guiho and J. P. Martinez-Barbera, Cell senescence in neuropathology: A focus on neurodegeneration and tumours, *Neuropathol. Appl. Neurobiol.*, 2021, **47**, 359.
17 L. Zhang, *et al.*, Cellular senescence: a key therapeutic target in aging and diseases, *J. Clin. Invest.*, 2022, **132**(15), e158450.
18 L. Wang, L. Lankhorst and R. Bernards, Exploiting senescence for the treatment of cancer, *Nat. Rev. Cancer*, 2022, **22**, 340–355.
19 M. Paez-Ribes, E. González-Gualda, G. J. Doherty and D. Muñoz-Espín, Targeting senescent cells in translational medicine, *EMBO Mol. Med.*, 2019, **11**, e10234.
20 D. Muñoz-Espín, Nanocarriers targeting senescent cells, *Transl. Med. Aging*, 2019, **3**, 1–5.
21 S. Chaib, T. Tchkonia and J. L. Kirkland, Cellular senescence and senolytics: the path to the clinic, *Nat. Med.*, 2022, **28**, 1556–1568.
22 J. L. Kirkland and T. Tchkonia, Senolytic drugs: from discovery to translation, *J. Intern. Med.*, 2020, **288**, 518–536.
23 J. Adamczyk-Grochala and A. Lewinska, Nano-Based Theranostic Tools for the Detection and Elimination of Senescent Cells, *Cells*, 2020, **9**, 2659.
24 A. Agostini, *et al.*, Targeted cargo delivery in senescent cells using capped mesoporous silica nanoparticles, *Angew. Chem., Int. Ed.*, 2012, **51**, 10556–10560.
25 D. Muñoz-Espín, *et al.*, A versatile drug delivery system targeting senescent cells, *EMBO Mol. Med.*, 2018, **10**, e9355.
26 N. Joudeh and D. Linke, Nanoparticle classification, physicochemical properties, characterization, and applications: a comprehensive review for biologists, *J. Nanobiotechnol.*, 2022, **20**, 262.
27 S. A. MacParland, *et al.*, Phenotype Determines Nanoparticle Uptake by Human Macrophages from Liver and Blood, *ACS Nano*, 2017, **11**, 2428–2443.
28 L. Wang, *et al.*, Administration route governs the therapeutic efficacy, biodistribution and macrophage targeting of anti-inflammatory nanoparticles in the lung, *J. Nanobiotechnol.*, 2021, **19**, 56.
29 L. Wang, *et al.*, Macrophage senescence in health and diseases, *Acta Pharm. Sin. B*, 2024, 1508–1524.
30 H. Zhu, F. Shen, T. Liao, H. Qian and Y. Liu, Immunosenescence and macrophages: From basics to therapeutics, *Int. J. Biochem. Cell Biol.*, 2023, **165**, 106479.
31 L. M. Pham, *et al.*, Targeting and clearance of senescent foamy macrophages and senescent endothelial cells by antibody-functionalized mesoporous silica nanoparticles for alleviating aorta atherosclerosis, *Biomaterials*, 2021, **269**, 120677.
32 L. Su, *et al.*, Potential role of senescent macrophages in radiation-induced pulmonary fibrosis, *Cell Death Dis.*, 2021, **12**, 1–12.
33 C. Erbel, *et al.*, An in vitro model to study heterogeneity of human macrophage differentiation and polarization, *J. Visualized Exp.*, 2013, e50332, DOI: 10.3791/50332.
34 X. Hu, Y. Zhang, T. Ding, J. Liu and H. Zhao, Multifunctional Gold Nanoparticles: A Novel Nanomaterial for Various Medical Applications and Biological Activities, *Front. Bioeng. Biotechnol.*, 2020, **8**, 990.
35 M. Ghebretatios, S. Schaly and S. Prakash, Nanoparticles in the Food Industry and Their Impact on Human Gut Microbiome and Diseases, *Int. J. Mol. Sci.*, 2021, **22**, 1942.
36 B. Jiang, *et al.*, Health impacts of environmental contamination of micro- and nanoplastics: a review, *Environ. Health Prev. Med.*, 2020, **25**, 29.
37 D.-W. Lee, *et al.*, Microplastic particles in human blood and their association with coagulation markers, *Sci. Rep.*, 2024, **14**, 30419.
38 H. A. Leslie, *et al.*, Discovery and quantification of plastic particle pollution in human blood, *Environ. Int.*, 2022, **163**, 107199.
39 K.-D. Wagner and N. Wagner, The Senescence Markers p16INK4A, p14ARF/p19ARF, and p21 in Organ Development and Homeostasis, *Cells*, 2022, **11**, 1966.
40 T. Tchkonia, Y. Zhu, J. van Deursen, J. Campisi and J. L. Kirkland, Cellular senescence and the senescent secretory phenotype: therapeutic opportunities, *J. Clin. Invest.*, 2013, **123**, 966–972.
41 J. Turkevich, G. Garton and P. C. Stevenson, The color of colloidal gold, *J. Colloid Sci.*, 1954, **9**, 26–35.
42 K. R. Brown and M. J. Natan, Hydroxylamine Seeding of Colloidal Au Nanoparticles in Solution and on Surfaces, *Langmuir*, 1998, **14**, 726–728.
43 A. M. Moreno-Echeverri, *et al.*, Pitfalls in methods to study colocalization of nanoparticles in mouse macrophage lysosomes, *J. Nanobiotechnol.*, 2022, **20**, 464.
44 E. Susnik, *et al.*, Increased Uptake of Silica Nanoparticles in Inflamed Macrophages but Not upon Co-Exposure to Micron-Sized Particles, *Cells*, 2020, **9**, 2099.
45 W. Stöber, A. Fink and E. Bohn, Controlled growth of monodisperse silica spheres in the micron size range, *J. Colloid Interface Sci.*, 1968, **26**, 62–69.
46 L. F. Muff, S. Balog, J. Adamcik, C. Weder and R. Lehner, Preparation of Well-Defined Fluorescent Nanoplastic Particles by Confined Impinging Jet Mixing, *Environ. Sci. Technol.*, 2023, **57**, 17201–17211.
47 E. Rebollar, *et al.*, Physicochemical modifications accompanying UV laser induced surface structures on poly(ethylene terephthalate) and their effect on adhesion of mesenchymal cells, *Phys. Chem. Chem. Phys.*, 2014, **16**, 17551–17559.

48 J. Schindelin, *et al.*, Fiji: an open-source platform for biological-image analysis, *Nat. Methods*, 2012, **9**, 676–682.
49 P. M. Hinderliter, *et al.*, ISDD: A computational model of particle sedimentation, diffusion and target cell dosimetry for in vitro toxicity studies, *Part. Fibre Toxicol.*, 2010, **7**, 36.
50 R. Kumari and P. Jat, Mechanisms of Cellular Senescence: Cell Cycle Arrest and Senescence Associated Secretory Phenotype, *Front. Cell Dev. Biol.*, 2021, **9**, 645593.
51 E. A. Kumah, *et al.*, Human and environmental impacts of nanoparticles: a scoping review of the current literature, *BMC Public Health*, 2023, **23**, 1059.
52 B. Chen, *et al.*, Silver nanoparticle-activated COX2/PGE2 axis involves alteration of lung cellular senescence *in vitro* and *in vivo*, *Ecotoxicol. Environ. Saf.*, 2020, **204**, 111070.
53 T. Spannbrucker, *et al.*, Induction of a senescent like phenotype and loss of gap junctional intercellular communication by carbon nanoparticle exposure of lung epithelial cells, *Exp. Gerontol.*, 2019, **117**, 106–112.
54 L. Ramos-Pan, *et al.*, Impact of gold nanoparticle exposure on genetic material, *Mutat. Res., Genet. Toxicol. Environ. Mutagen.*, 2024, **900**, 503827.
55 P. Falagan-Lotsch, E. M. Grzincic and C. J. Murphy, One low-dose exposure of gold nanoparticles induces long-term changes in human cells, *Proc. Natl. Acad. Sci. U. S. A.*, 2016, **113**, 13318–13323.
56 M. A. Khan and M. J. Khan, Nano-gold displayed anti-inflammatory property via NF-kB pathways by suppressing COX-2 activity, *Artif. Cells, Nanomed., Biotechnol.*, 2018, **46**, 1149–1158.
57 L. Shang, K. Nienhaus and G. U. Nienhaus, Engineered nanoparticles interacting with cells: size matters, *J. Nanobiotechnol.*, 2014, **12**, 5.
58 Y.-Y. Liu, *et al.*, On the Cellular Uptake and Exocytosis of Carbon Dots–Significant Cell Type Dependence and Effects of Cell Division, *ACS Appl. Bio Mater.*, 2022, **5**(9), 4378–4389.
59 Y.-Y. Liu, *et al.*, Fate of CdSe/ZnS quantum dots in cells: Endocytosis, translocation and exocytosis, *Colloids Surf., B*, 2021, **208**, 112140.
60 R. Ahijado-Guzmán, *et al.*, Intercellular Trafficking of Gold Nanostars in Uveal Melanoma Cells for Plasmonic Photothermal Therapy, *Nanomaterials*, 2020, **10**, 590.
61 W. Liu, *et al.*, Aggregation and aging of nanoparticle–protein complexes at interfaces studied by evanescent-light scattering microscopy, *Aggregate*, 2024, **5**, e538.
62 H. Tang, H. Ye, H. Zhang and Y. Zheng, Aggregation of nanoparticles regulated by mechanical properties of nanoparticle-membrane system, *Nanotechnology*, 2018, **29**, 405102.
63 A. B. Chinen, C. M. Guan, C. H. Ko and C. A. Mirkin, The Impact of Protein Corona Formation on the Macrophage Cellular Uptake and Biodistribution of Spherical Nucleic Acids, *Small*, 2017, **13**, 1603847.
64 J. A. Kim, *et al.*, Low Dose of Amino-Modified Nanoparticles Induces Cell Cycle Arrest, *ACS Nano*, 2013, **7**, 7483–7494.
65 S.-A. Yang, S. Choi, S. M. Jeon and J. Yu, Silica nanoparticle stability in biological media revisited, *Sci. Rep.*, 2018, **8**, 185.
66 E. J. Márquez, *et al.*, Sexual-dimorphism in human immune system aging, *Nat. Commun.*, 2020, **11**, 751.
67 J. R. Yarbro, R. S. Emmons and B. D. Pence, Macrophage Immunometabolism and Inflammaging: Roles of Mitochondrial Dysfunction, Cellular Senescence, CD38, and NAD, *Immunometabolism*, 2020, **2**, e200026.
68 P. Foroozandeh, A. A. Aziz and M. Mahmoudi, Effect of Cell Age on Uptake and Toxicity of Nanoparticles: The Overlooked Factor at the Nanobio Interface, *ACS Appl. Mater. Interfaces*, 2019, **11**, 39672–39687.